Transition dynamics in two-photon ionisation

Morgane Vacher, Romain Gaillac, Alfred Maquet, Richard Taïeb, Jérémie Caillat

Transition dynamics in two-photon ionisation

Morgane Vacher[1,2], Romain Gaillac[1,3*], Alfred Maquet[1], Richard Taïeb[1], and Jérémie Caillat[1†]
[1] *Sorbonne Université, UPMC Université Paris 6, UMR 7614, Laboratoire de Chimie Physique–Matière et Rayonnement, 4, place Jussieu 75231 Paris Cedex 05, France, and CNRS, UMR 7614, LCPMR, Paris, France*
[2] *Department of Chemistry – Ångström, Uppsala University, Box 538, 751 21 Uppsala, Sweden*
[3] *Department of Chemistry, École Normale Supérieure, 24, rue Lhomond, 75005 Paris, France*

We review various aspects of photoemission dynamics in the case of 2-photon ionisation. We first recall the definition of a transition phase specific to 2-photon transitions. Numerical experiments on model atoms are used to show how the group delay associated with the transition phase is actually representative of the early dynamics of the detected photoelectron wave packets. Then we address the question of measuring these transition delays using a standard interferometric technique of experimental attosecond physics, so-called RABBIT. Finally, we outline different reinterpretations of RABBIT giving access to the more fundamental scattering dynamics affecting any photoemission process.

Compiled: Tuesday 17th October, 2017, 12:38

Contents

I. INTRODUCTION

Two-photon ionisation is an essential process in attosecond science [1, 2], invoked at various stages of a number of experimental schemes developped for attosecond time-resolved spectroscopy.

The first characterisations of XUV attosecond light pulses in 2001 [3, 4] were achieved using XUV-IR two photon interferometry, where the IR plays the role of a probe field setting an external clock for the temporal reconstruction of XUV bursts produced by high harmonic generation (HHG) [5, 6]. These pioneer experiments have laid the foundations of two classes of characterisation setups – the so-called *streaking* technique adapted to single attosecond pulses [7, 8] and RABBIT[1] scheme adapted to attosecond pulse trains [9, 10]. They have become, since then, standard methods of attosecond technology. Beyond characterisation, the development of these techniques opened the way for coherent control and shaping of attosecond light pulses [11–14], as well as for a new class of spectroscopy (dubbed high harmonic spectroscopy), which consists in analysing the HHG radiation

*Present address: IRCP, Chimie ParisTech, 11 rue Pierre et Marie Curie, 75005 Paris, France
†Electronic address: jeremie.caillat@upmc.fr

[1] RABBIT stands for Reconstruction of Attosecond Beatings By Interference of Two-photon transitions [10].

to retrieve spatial and temporal information on the generating medium itself with unprecedented, combined Å and sub-fs resolutions [15].

In the wide variety of attosecond resolved experiments developped over the years, two-photon processes have also been used in more conventional pump-probe schemes, in order to trigger and/or to probe ultrafast dynamics in chemical matter. Among these, thought-provoking experiments have revisited in the time domain the process of photoemission itself, evidencing ionisation delays ranging from few attoseconds to few femtoseconds in atoms [16, 17], molecules [18] and solids [19]. These measurements unfold an intuitive [20] yet up-to-then confidential point of view on a very fundamental process of quantum physics and spectroscopy, and they initiated a considerable amount of subsequent theoretical and experimental work, see *e.g.* the reviews [21–23].

The present article focuses on the imprints that are characteristic to two-photon transitions on photoelectron dynamics. In part II, using well-established second-order perturbation theory, we provide a formal definition for a "transition delay", introduced as the group delay associated with the contribution of the transition operator to the overall photoelectron phase. Then, we show in part III that this formal group delay is indeed representative of the actual early-stage dynamics of the detected photoelectron. We used for this numerical experiments performed on low dimensional model systems. Finally, part IV reviews the principles of the RABBIT interferometry and highlights the way it provides access to photoemission dynamics at various levels of approximations. Here as well, the validity of the approaches are illustrated with numerical simulations. This is followed by a conclusion in part V.

II. TRANSITION PHASE AND TRANSITION GROUP DELAY

A. Formal definition of a 2-photon transition delay

1. *Second order perturbation theory for monochromatic fields*

The interaction of an atom or a molecule with two photons from different fields may induce, in the most general case, transitions leading to four different final energies – where each photon is either absorbed or emitted. Here we consider photoemission processes, which restricts us to situations where at least one of the photons is absorbed (the most energetic one, with angular frequency ω_a). The other photon (with angular frequency $\omega_b < \omega_a$) is either absorbed or emitted. The photoelectron energy E therefore reads

$$E = E_{\rm ini} + \hbar\omega_a \pm \hbar\omega_b > 0 \tag{1}$$

where $E_{\rm ini}$ is the initial bound state energy, the origin being set at the ionisation threshold.

Second order perturbation theory expresses the amplitude associated to such a transition, from an initial state $|\psi_{\rm ini}\rangle$ to a given final state $|\psi_{E,\rm fin}\rangle$, as the matrix element

$$T(\omega_a, \pm\omega_b) = \langle\psi_{E,\rm fin}|\hat{\rm T}(\omega_a, \pm\omega_b)|\psi_{\rm ini}\rangle \tag{2}$$

involving the transition operator

$$\hat{\rm T}(\omega_a, \pm\omega_b) = \left[(\vec{\epsilon}_b\cdot\hat{\mathbf{r}})\hat{\rm G}(\omega_a)(\vec{\epsilon}_a\cdot\hat{\mathbf{r}}) + (\vec{\epsilon}_a\cdot\hat{\mathbf{r}})\hat{\rm G}(\pm\omega_b)(\vec{\epsilon}_b\cdot\hat{\mathbf{r}})\right] \times F_a e^{i\phi_a} F_b e^{\pm i\phi_b}. \tag{3}$$

F_k and ϕ_k represent the amplitude and phase of the electric field at pulsation ω_k ($k = a, b$), $\vec{\epsilon}_a$ and $\vec{\epsilon}_b$ the corresponding polarisation directions and

$$\hat{\rm G}(\omega) = \lim_{\zeta\to 0^+} \frac{1}{E_{\rm ini} + \hbar\omega - \hat{\rm H} + i\zeta} \tag{4}$$

is the Green's operator, where $\hat{\rm H}$ is the system's field-free hamiltonian. Each of the two terms contributing to $\hat{\rm T}(\omega_a, \pm\omega_b)$ is usually assigned a proper chronology: absorption of photon ω_a followed by absorption/emission of photon ω_b on the one hand; absorption/emission of photon ω_b followed by absorption of photon ω_a on the other hand.

The transition dynamics can further be characterised by a group delay derived from the phase accumulated by the photoelectron before reaching the final state. The latter phase is formally evidenced by expanding the Green's operator on an eigenbasis $\{|\psi_n\rangle\}$ of $\hat{\rm H}$ (with eigenvalues E_n),

$$\hat{\rm G}(\omega) = \lim_{\zeta\to 0^+} \sum\!\!\!\!\!\!\int_n \frac{|\psi_n\rangle\langle\psi_n|}{E_{\rm ini} + \hbar\omega - E_n + i\zeta}, \tag{5}$$

the (multi)-index n covering both the discrete and continuum parts of the spectrum. If one of the photons brings the system above the ionisation threshold, there exists an eigen-energy $E_{\bar{n}}$ for which $E_{\rm ini} + \hbar\omega - E_{\bar{n}} = 0$, making the integral in Eq. 5 singular. The operator then takes the form:

$$\hat{\rm G}(\omega) = \mathcal{P}\frac{1}{E_{\rm ini} + \hbar\omega - \hat{\rm H}} - i\pi\delta(E_{\rm ini} + \hbar\omega - \hat{\rm H}), \tag{6}$$

where $\mathcal{P}$ designates Cauchy's principal part.

Thus, the transition operator is *complex* as soon as the system can be ionised by one of the photons alone. This brings a phase to the matrix element $T(\omega_a, \pm\omega_b)$ in addition to the phase $\phi_a \pm \phi_b$ inherited from the driving fields, which sets an external clock to the process. Note that the scattering phase $\eta_{\rm sc}$ of the photoelectron also contributes to $\arg T$ when the final state is described by a complex valued scattering wave function. However, the present article focuses on the time-domain interpretation of the contribution of the transition itself to the phase accumulated by the photoelectron, in a given photoemission channel. For this reason, we will use throughout this study *real-valued* continuum wave

functions, which encode the final state scattering phase in their asymptotic oscillations (see *e.g.* [24, 25]).

Below, we see how to account for the spectral width of the ionising pulses, and the consequences on the identification of a "transition phase" among the contributions to the overall phase accumulated by the photoelectron wave packet.

2. Accounting for the pulse durations

When dealing with pulses of finite durations, the actual spectral amplitudes $\mathcal{T}(E)$ of the created electron wave packet (EWP) are obtained by integrating the amplitude defined in Eq. 2 over all the possible photon pairs leading to the final state at each energy E (see *e.g.* [26]):

$$\mathcal{T}(E) \;=\; \int_{-\infty}^{+\infty} T(\omega_a, \pm\omega_b)\,\mathrm{d}\omega_a \tag{7}$$

with the energy conservation constraint $\pm\omega_b = (E - E_{\mathrm{ini}})/\hbar - \omega_a$. Note that each pair of photon frequencies brings a factor $F_a e^{i\phi_a} F_b e^{i\phi_b}$, included in the expression of $T(\omega_a, \pm\omega_b)$, under the integral. This issue is of particular importance, since the integration in Eq. 7 entangles, in the most general case, the "atomic" contribution (imprinted by $\hat{\mathrm{G}}$ in Eq. 3) and the field contributions to the EWP amplitude $\mathcal{T}(E)$ and its phase

$$\Theta \;=\; \arg \mathcal{T}(E). \tag{8}$$

Separating the contributions to Θ is however mandatory for the interpretation of most of the recent attosecond resolved pump-probe experiments using 2-photon transitions, notably RABBIT-based schemes (see Section IV). It is in practice possible when (i) the two ionising fields display constant phases within their bandwidths, or (ii) when one of the pulses is spectrally narrow enough to discard the integration, assuming the two components to display no spectral overlap. In such cases, one identifies the contribution to Θ that is specific to the ionised chemical species (so-called "atomic", "molecular" or "transition" phase) as

$$\theta \;=\; \Theta - (\phi_a \pm \phi_b). \tag{9}$$

The above-mentionned RABBIT interferometric method, based on XUV-IR two-photon transitions, assumes in its common implementations a narrow IR pulse.

To the transition phase one associates a "transition delay" defined as the group delay

$$\tau \;=\; \hbar \frac{\partial \theta}{\partial E}, \tag{10}$$

in analogy with the Wigner delay associated to the scattering phase η_{sc} accumulated in the final continuum state [16, 17, 20, 24, 27]. The transition delay is the time-domain quantity the present study is focused on.

B. An illustrative case: 2-photon transition through an isolated resonance

The relevance of the group delay defined in Eq. 10 to characterise the actual transition dynamics can be illustrated with the specific case of a resonant two-photon transition. For this, let us consider an atom or a molecule displaying a resonance in the vicinity of the region reached by the photon ω_a, *ie* at energy $E_{\mathrm{R}} \approx E_{\mathrm{ini}} + \hbar\omega_a$. We note Γ_{R} the width of the resonance. For simplicity, we assume monochromatic pulses and work directly on the transition amplitudes $T(\omega_a, \pm\omega_b)$, ignoring the integration over the pulse widths (Eq. 7). We additionally consider the resonance to be significantly intense and isolated, such that all the contributions to $T(\omega_a, \pm\omega_b)$ are dominated by the transition path involving the resonance as the intermediate state,

$$\begin{aligned} T(\omega_a, \pm\omega_b) \;\simeq\; & \frac{\langle \psi_{E,\mathrm{fin}} | \vec{\epsilon}_b \cdot \hat{\mathbf{r}} | \psi_{\mathrm{R}} \rangle \langle \psi_{\mathrm{R}} | \vec{\epsilon}_a \cdot \hat{\mathbf{r}} | \psi_{\mathrm{ini}} \rangle}{\hbar\Delta\omega_a + i\Gamma_{\mathrm{R}}} \\ & \times F_a e^{i\phi_a} F_b e^{\pm i\phi_b} \end{aligned} \tag{11}$$

In this approximate expression, $\hbar\Delta\omega_a = E_{\mathrm{ini}} + \hbar\omega_a - E_{\mathrm{R}}$ is the detuning of the "first" photon with respect to the resonance. The angular frequency of the "second" photon, ω_b, shows up implicitly through the energy conservation law given in Eq. 1. The transition phase

$$\theta \;\simeq\; \arctan\left(-\frac{\Gamma_{\mathrm{R}}}{\hbar\Delta\omega_a}\right) \tag{12}$$

depends explicitly on ω_a only. When scanning the resonance by varying $\Delta\omega_a$, the group delay defined in Eq. 10 now reads

$$\tau \;\simeq\; \frac{\partial\theta}{\partial\omega_a} \tag{13}$$

$$\;\simeq\; \hbar \frac{\Gamma_{\mathrm{R}}}{\Gamma_{\mathrm{R}}^2 + (\hbar\Delta\omega_a)^2}. \tag{14}$$

It varies between 0 (large $|\Delta\omega_a|$) and the resonance lifetime $\tau_{\mathrm{R}} = \hbar\Gamma_{\mathrm{R}}^{-1}$ ($\Delta\omega_a = 0$), and it is always positive. In this case, the delay can be interpreted as the *duration* of the transition, which reduces to the following chronology: (i) photon ω_a is absorbed, (ii) the system remains in the intermediate resonance for a characteristic duration τ and (iii) it absorbs/emits photon ω_b[2].

One should keep in mind that interpreting the transition group delay as a *duration* holds in particular situations where a single resonant path, among all those open according to Eqs. 3 and 5, significantly contributes to the transition amplitude. In a more general framework,

[2] A comprehensive and rigorous derivation of transition durations in the context of resonant Raman spectroscopy can be found in [28], exploited *e.g.* for probing the ultrafast dissociation of small molecules in excited states [29].

as considered in the numerical simulations presented in section III, the group delay reflects the temporal (and inherently, spectral) distorsions of the produced EWP as compared to the ionising pulse profiles.

The above derivation also illustrates the close relationship between the 2-photon transition group delay and the scattering delay experienced by the electron ending up in the intermediate state, here characterised by the resonance lifetime τ_R. This fundamental connection is the cornerstone of 2-photon pump-probe setups developed in the past few years to access the scattering dynamics subsequent to 1-photon ionisation [27], see Section IV C.

III. TRANSITION DELAY AND PHOTOELECTRON WAVE PACKET DYNAMICS

To demonstrate how the above defined transition phase and the associated group delay characterise the actual photoemission dynamics, we performed numerical simulations in simple model systems, following an approach similar to the one used in [21, 24] in the context of one-photon transitions. We simulated the full ionisation dynamics by solving the time-dependent Schrödinger equation (TDSE) for the model systems in presence of the fields, and confronted it to the formal delays derived from transition amplitudes obtained using second order perturbation theory.

A. Model systems

1. Potentials

Our numerical experiments were performed on model 1D atoms made of a single electron, of coordinate x, in various (symmetric) potentials. Each considered potential is constructed as the sum

$$V(x) = V_{LR}(x) + V_{SR}(x) \tag{15}$$

of a long range soft-Coulomb interaction,

$$V_{LR}(x) = -\frac{e^2}{4\pi\epsilon_0}\frac{1}{\sqrt{x^2+a^2}}, \tag{16}$$

and a system-specific short range contribution $V_{SR}(x)$. The long range contribution reproduces the universal asymptotic tail of the potential felt by a photoelectron leaving a singly charged ion. Its screening parameter a is the main knob to adjust the ground state energy. The short range term $V_{SR}(x)$ accounts qualitatively for the interactions between the active electron and the ion core at short distances, and decays faster than $1/|x|$. It provides a flexible way of structuring the continuum.

In the following, we report results obtained on three model systems, dubbed A, B and C, and referred to as "atoms" in the following for simplicity. All have their ground state energy E_0 set to −15.64 eV. Atom A is built with the long range potential only [$V_{SR}(x) = 0$], while the potentials of atoms B and C display additional, symmetric, short-range barriers. In both cases, the barrier separation was adjusted to induce a shape resonance at $E_R \simeq 1.9$ eV above threshold. The main difference between atoms B and C is the resonance lifetime $\hbar\Gamma_R^{-1}$, set to 1.7 fs and 54.8 fs respectively. The corresponding potentials are shown in Fig. 1 and their main characteristics are reported in Table I.

model atom	a (a.u.)	x_B (a.u.)	w_B (a.u.)	V_B (eV)	E_0 (eV)	E_R (eV)	Γ_R (meV)	$\hbar\Gamma_R^{-1}$ (fs)
A	1.2	–	–	–	−15.64	–	–	–
B	1.2	±7.50	5.0	1.36	−15.64	+1.86	387	1.7
C	1.2	±9.25	7.5	3.54	−15.64	+1.87	12	54.8

TABLE I: Parameters defining each model atom used in our simulations: a is the regularisation parameter for the soft-Coulomb long-range component [$V_{LR}(x)$]; x_B, w_B and V_B represent the central position, the width and the height of the hyper-gaussian barriers shaping the short range contribution [$V_{SR}(x)$] in atoms B and C. The ground state energy E_0, as well as the resonance energy E_R, width Γ_R (and lifetime $\hbar\Gamma_R^{-1}$) are the relevant properties for the present study.

2. Wave function parity and selection rule

The three atoms being built on symmetric potentials, their bound eigenstates have defined and alternate parities, starting with an even wave function for the ground state. This point is crucial for the following, since the selection rule in 1D allows 1-photon transitions only between states of opposite parities. As a consequence, any transition from an initial eigenstate of these systems occurs through a single channel. The above-mentioned resonances in atoms B and C have odd wave functions.

3. Adapted references

The definition of a *delay* inherently comes with the choice of a *reference*. Since the group delay considered here is related to the transition phase θ defined in Eq. 9, an absolute reference is provided by a transition for which the spectral variations of the transition phase are zero – which is the case of single-photon transitions. Most importantly, the reference transition must lead to the same final state $|\psi_{E,\mathrm{fin}}\rangle$ in order to exclude the scattering contribution from the studied dynamics. In time-dependent simulations, we will therefore compare each 2-photon transition starting from the ground state of a given model atom, to a 1-photon transition starting from the first excited state of the same atom, and ending up exactly at the same energies.

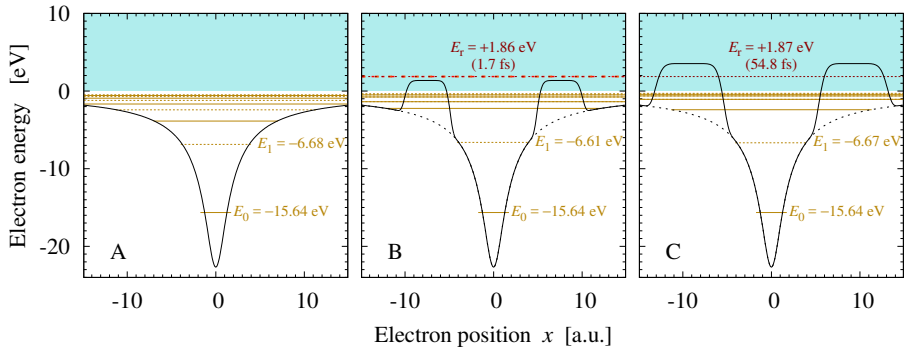

FIG. 1: (color online) Model potentials used in our simulations. The potential for model atom A (left) consists in a simple soft-Coulomb potential. The potentials for atoms B (center) and C (right) are augmented with additional barriers structuring the continuum. Horizontal lines indicate discrete energy levels: bound states ($E < 0$, yellow) and resonances ($E > 0$, red). The line styles are associated with the parity of each state: even (full) or odd (dashed). The energy (and life-time) of the states relevant for our study are also indicated. The main parameters defining these potentials are reported in Table I.

4. *Light pulses*

The light pulses considered in our simulations are defined in the time-domain using vector potentials

$$A(t) = \sum_{k=1}^{n_c} A_k f(T_k, \tau_k, t) \cos[\bar{\omega}_k (t - \tau_k) + \tilde{\phi}_k]. \quad (17)$$

In this generic expression, the sum runs over the number n_c of "colours" that constitute the complete pulse. Each component is characterised by a central frequency $\bar{\omega}_k$, a carrier-envelop phase (CEP) $\tilde{\phi}_k$, an amplitude A_k and a $\sin^2$ envelop f of duration T_k (full width at half maximum, FWHM), centered at time τ_k.

For the time-independent perturbative computations, we used the spectral counterpart of the electric field associated with the above defined vector potential.

B. Influence of the intermediate states

The simulations presented here illustrate to which extent the transition group delay defined in Eq. 10 for 2-photon ionisation is representative of the actual photoelectron dynamics, with a highlight on the imprint of the intermediate states.

We used two-color pulses ($n_{\rm col} = 2$ in Eq. 17, each color labeled a and b in the following) lasting $\simeq 20$ fs FWHM. For simplicity, we considered the pulses to be unchirped ($\tilde{\phi}_a = \tilde{\phi}_b = 0$ in Eq. 17) and both centered at the time origin ($\tau_a = \tau_b = 0$), such that $\Theta = \theta$ (see Eq. 9).

1. *Two-photon transitions through a broad resonance*

We first detail our procedure with the simulations performed on atom B, photoionised by light pulses of central energies $\hbar\bar{\omega}_a = 17.5$ eV and $\hbar\bar{\omega}_b = 4.9$ eV respectively. The frequency $\bar{\omega}_a$ was adjusted to bring the system in the vicinity of the shape resonance lying 1.86 eV above threshold. We focus on the photoelectron wave packet formed upon absorption of two photons, emitted with a central energy $\simeq 6.8$ eV.

The main task to compute transition group delays as defined in Eq. 10 consists in evaluating the wave packet amplitudes $\mathcal{T}(E)$ (Eq. 7). To this end, we evaluated the two-photon transition amplitudes $T(\omega_a, \pm\omega_b)$ (Eq. 2) *via* the computation of the first order perturbed wave function [30], a method that notably bypasses the explicit integration over the whole intermediate spectrum (Eq. 5). Figure 2(a) shows the corresponding electron spectrum

$$\sigma(E) = |\mathcal{T}(E)|^2 \quad (18)$$

and transition phase $\theta(E) = \arg \mathcal{T}(E)$. The spectrum displays a smooth bell shaped profile, which mostly reflects the pulse spectral envelops. The average energy under the peak,

$$\bar{E} = \frac{\int E \times \sigma(E)\, \mathrm{d}E}{\int \sigma(E)\, \mathrm{d}E}, \quad (19)$$

is 6.76 eV [$\simeq E_0 + \hbar(\bar{\omega}_1 + \bar{\omega}_2)$]. Within this peak, the transition phase varies linearly. Its spectral derivative evaluated at the average energy $\bar{E}$ provides a group delay

$$\tau = \hbar \frac{\partial \theta(E)}{\partial E}\bigg|_{\bar{E}} \quad (20)$$

amounting to 0.955 fs.

From a different perspective, we solved numerically the TDSE for the same atom interacting with the equivalent pulses in the time domain. We characterised the photoemission dynamics by computing the outgoing electron flux at a given position $x_{\rm d}$ [24],

$$j_{\rm out}(x_{\rm d}, t) = \Re{\rm e}\left\{ -\frac{i\hbar}{m} \psi^\star(x_{\rm d}, t) \left.\frac{\partial \psi(x,t)}{\partial x}\right|_{x_{\rm d}} \right\} \times \frac{x_{\rm d}}{|x_{\rm d}|} \quad (21)$$

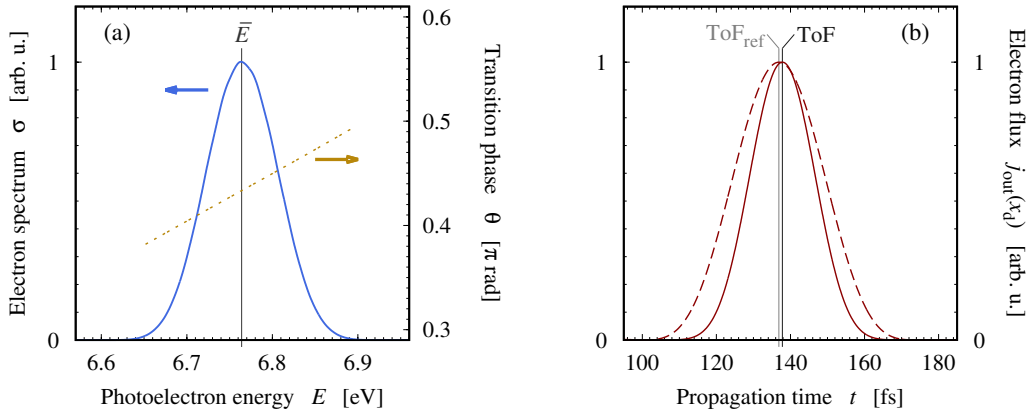

FIG. 2: (color online) Electron wave packet created by 2-photon ionisation of atom B using pulses with central energies $\hbar\bar{\omega}_a$ = 17.5 eV and $\hbar\bar{\omega}_b$ = 4.9 eV. (a) Electron spectrum σ (blue line) and phase θ of the transition amplitude computed using second order perturbation theory (yellow dotted line) as a function of the photoelectron energy E. $\bar{E}$ corresponds to the average energy under the peak (vertical line). (b) Outgoing photoelectron flux computed at x_d = 4000 a.u. as a function of time for the considered 2-photon transition (full red curve) and for the reference 1-photon transition starting from the first excited state and ending at the same average energy $\bar{E}$ (dashed red curve). ToF and ToF$_{ref}$ (vertical lines) are the average numerical times of flight towards the virtual detector in the two systems respectively. Their difference (ΔToF = 0.945 fs) is significant, in spite of being small compared to the wave packet temporal extensions at detection (several tens of fs).

where ψ is the solution of the TDSE, $\psi^\star$ its complex conjugate. In order to restrain our analysis to the same photoelectron peak as in the time-independent computations, we filtered the wave function by applying an appropriate spectral mask prior to the flux analysis. Fig. 2(b) shows the flux obtained at x_d = 4000 a.u. This distance is at the same time large enough to let the pulses vanish before the EWP covers it and small enough to prevent a too pronounced spreading of the wave packet. As in the spectral domain, the resulting flux displays a smooth bell shaped profile. The average time-of-flight (ToF) towards the virtual detector,

$$\text{ToF} = \frac{\int t \times j_{out}(x_d,t)\,dt}{\int j_{out}(x_d,t)\,dt}, \tag{22}$$

is here 137.8 fs. It is close to the 137.3 fs it would take a free electron with kinetic energy $\bar{E}$ to cover the distance of 4000 a.u. We obtained an absolute reference for this timing by simulating the interaction of atom B initially in its first excited state, with a single pulse of roughly 13.35 eV, finely tuned to reach the same final energy $\bar{E}$ as in the two-photon simulations. The obtained reference flux is also displayed in Fig. 2(b). It presents a similarly smooth shape (apart from being slightly broader, due to a longer pulse duration). The corresponding time-of-flight ToF$_{ref}$ = 136.9 fs is slightly shorter than the one obtained previously. This indicates that the EWP is effectively *delayed* by the two-photon transition, as compared to the one produced by an instantaneous 1-photon transition[3].

[3] The fact that ToF$_{ref}$ is even shorter than the free electron ToF simply results from the attractive Coulomb potential, which accelerates the electron at all distances for a given total energy.

The two-photon transition delay given by these times-of-flight,

$$\Delta\text{ToF} = \text{ToF}(x_d) - \text{ToF}_{ref}(x_d), \tag{23}$$

is equal to 0.945 fs, which is very close to the group delay inferred from the perturbative transition amplitudes (Eq. 20). We have further checked that this value is fairly insensitive to the virtual detector position. The fact that the wave packet dynamics is well represented by a single characteristic time – a delay – is consistent with a phase varying linearly under a bell shaped peak in the spectral domain [Fig. 2(a)]. The $\simeq$ 10 as discrepancy observed between the two evaluations of this delay results from a slight distorsion induced by the resonance, which is here exactly reached by one of the photons. We will see below that this discrepancy vanishes as soon as the photon frequencies depart from the resonance.

To emphasise the influence of the intermediate resonance on the transition dynamics, we repeated the procedure with different values of $\hbar\bar{\omega}_a$ ranging from 16.6 to 18.7 eV while keeping the sum $\hbar(\bar{\omega}_a + \bar{\omega}_b)$ equal to 22.4 eV. The delays ΔToF (Eq. 23) and the group delays τ (Eq. 20) are reported in Fig. 3(b) as functions of $\hbar\bar{\omega}_a$. The two sets of data are in excellent agreement. They follow a lorentzian curve peaking at $\hbar\bar{\omega}_a = E_R - E_0$, reproducing qualitatively the behaviour predicted by the formula given in Eq. 14 (valid for monochromatic fields and when only the resonance transiently contributes to the 2-photon transition). At resonance, the transition is dominated by the sequence where the ω_a photon is absorbed before the ω_b photon. The transition delay may then be interpreted as a transition *duration* corresponding to a characteristic time spent by the system in the resonance before it absorbs the second photon. The maximum delay ($\simeq$ 1 fs) is lower than the resonance lifetime,

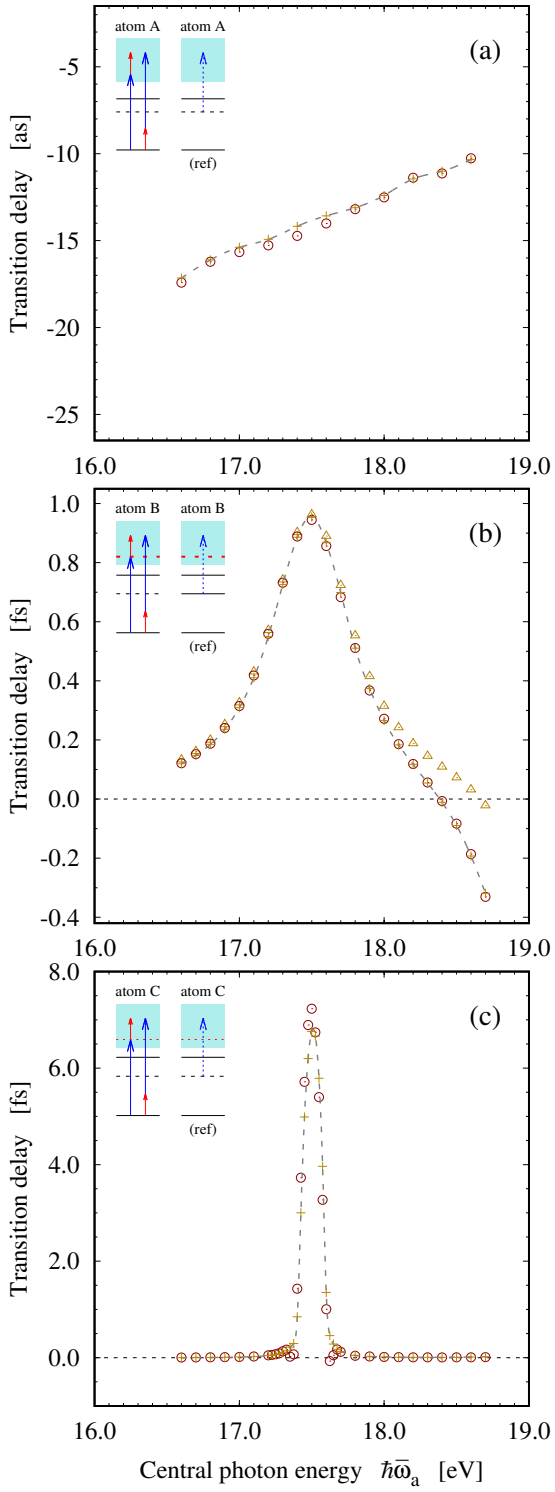

FIG. 3: (color online) 2-photon transition dynamics evidenced in the three model atoms ($\hbar\bar{\omega}_a + \hbar\bar{\omega}_b$ = 22.4 eV): group delay τ (yellow crosses) and time of flight differences ΔToF (red circles) as functions of $\hbar\bar{\omega}_a$, evidenced (a) in a smooth continuum (atom A), (b) in presence of a broad resonance (atom B), and (c) in presence of a narrow resonance (atom C). The yellow triangles in panel (b) correspond to the group delay τ derived from the amplitude computed with the resonant paths *only* ($\omega_a + \omega_b$), and neglecting the alternative path ($\omega_b + \omega_a$).

because of the integration of the transition amplitudes $T(\omega_a, \pm\omega_b)$ (Eq. 2) over the pulse widths (Eq. 7). This reflects the fact that the transition delay is indeed induced by the intermediate resonance, yet obviously limited by the pulse durations.

We have further confirmed the preponderant role of the $\omega_a + \omega_b$ sequences by recomputing the transition amplitudes *excluding* the complementary $\omega_b + \omega_a$ sequences. The corresponding group delays τ are also displayed in Fig. 3. They are indeed very close to the ones derived from the complete amplitudes close to resonance. However, discrepancies become noticeable at larger $\hbar\bar{\omega}_a$, indicating that the $\omega_b + \omega_a$ sequence cannot in general be left aside neither from the computation nor from the interpretation of the transition group delay. One faces here the limitation of interpreting these delays in terms of "durations", as already mentioned at the end of Section II A: The computed delays take negative values when $\hbar\bar{\omega}_a$ gets away from the resonance, while a duration is by essence positive – a misinterpretation in such cases typically leads to the awkward notion of "faster than light" processes, see also [31].

2. ... through a narrow resonance

We followed the same approach with atom C, which displays a narrower resonance (lifetime of 54.8 fs) at nearly the same energy. The ToF differences and the group delays are reported in Fig. 3(c). The maximum delay reached at resonance ($\simeq$ 7 fs) is much smaller than the actual lifetime, a direct signature of the strong temporal gating of the process by the pulse durations. Here as well, the two sets of data are in very good agreement. A discrepancy of $\sim$ 0.5 fs is nevertheless observed at resonance, when the delay is maximum. This results from a more pronounced distorsion of the EWP due to the resonance, both in the spectral and temporal domains (not shown) – distorsion that cannot be completely accounted for by a simple group delay. Note that these discrepancies are much less pronounced than when performing the same analysis for 1-photon transitions. Indeed, an EWP created by a resonant 1-photon transition displays in the time domain an exponentially decaying tail $\propto \exp(-\Gamma_R t/\hbar)$, which is poorly represented by a single group delay. In a study reported in [21], 1-photon simulations performed on the same model atom with 25 fs pulses (FWHM) provided a ΔToF of $\simeq$ 30 fs at resonance, while the group delay τ corresponds exactly to the resonance lifetime, $\simeq$ 55 fs (see Figs. 8.3 and 8.4(c) of this reference). In the present work, the bell-shape of the resonant wave packet is fairly preserved due to the finite duration of the additional pulse accounted for in Eq. 7, as already mentioned.

3. … and through a smooth continuum

Finally, the same simulations were carried out on atom A, which presents a smooth continuum. The results are shown in Fig. 3(a). The transition delay takes here negative values and monotonically goes to 0 when $\hbar\bar{\omega}_a$ increases. This is a signature of the way electron wave packets build up *via* the filter of a density of states slowly decaying as $\propto 1/\sqrt{2E}$ [32]. The observed discrepancies between Δ_{ToF} and τ are of the order the numerical accuracy: They are visible in this figure because the time range over which the delays vary is very narrow, covering less than 20 as, while the detected wave packets spread over several tens of fs.

With this last example, one should note that the 2-photon transition delays are particularly small, especially away from the threshold, as long as no long-lived intermediate resonance significantly affects the build-up of the EWP. This property is exploited by the streaking and RABBIT techniques in their initial designs, which consist in characterising XUV light pulses with sub-fs resolutions by means of XUV-IR 2-photon transitions. The next section is dedicated to the RABBIT technique in particular, and to its recent reinterpretations for the investigation of photoemission dynamics.

IV. INTERFEROMETRIC MEASUREMENTS

Resolving dynamics on the attosecond or femtosecond time scales directly in the time domain is way beyond the capacities of experimental detectors. Up to now, photoemission dynamics has thus been accessed in experiments using interferometric methods, providing photoelectron wave packet amplitudes and phases in the spectral domain. We focus here on the RABBIT technique, which directly measures the two-photon transition amplitudes encoding the transition dynamics discussed previously.

A. The RABBIT technique

1. The interferometer

The RABBIT technique exploits the main properties of the radiation produced by HHG: (i) it spans a broad spectrum ranging from the IR to the XUV domains, (ii) its spectrum is composed of *odd* harmonics of the generating fundamental IR field, (iii) the radiation is *coherent*. In RABBIT, a target (typically a gas) is photoionised by a comb of odd harmonics produced by HHG, in presence of a fraction of IR field (of frequency ω_{L}) diverted from the generating source.

A typical RABBIT electron spectrum is represented in Fig. 4. It displays a series of peaks associated with each harmonic constituting the XUV comb, centred at the energies $-I_p + (2q+1)\times\hbar\omega_{\text{L}}$ ($q \in \mathbb{N}$) where I_p is the target's ionisation potential. In the following, these "harmonic" peaks are labelled H_{2q-1}, H_{2q+1} … The presence of the IR fields induces additional peaks resulting from 2-photon transions: absorption of an XUV photon and absorption or emission of an IR photon. Since the XUV field is made of *odd* harmonics of the dressing IR, these sidebands are centred between the harmonic peaks, at the energies $-I_p + 2q\times\hbar\omega_{\text{L}}$. Moreover, the frequency relationship between the involved XUV and IR photons is such that two different paths lead to a given sideband SB_{2q}: (i) absorption of harmonic $(2q-1)$ and *absorption* of an IR photon, and (ii) absorption of harmonic $(2q+1)$ and *stimulated emission* of an IR photon. Since the XUV and IR radiations are coherent, the two paths interfere in the population of the final state. Their spectral profile, for each photoelectron energy, thus may be expressed in the very general form [10, 33]:

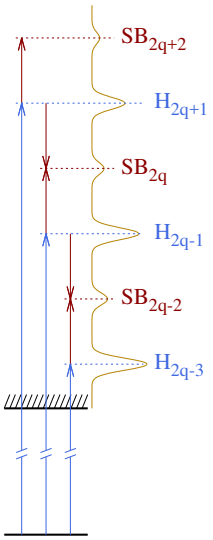

FIG. 4: (color online) Photoionisation of a gas by an XUV comb produced by HHG (odd order harmonics of an IR field, blue arrows) in presence of the fundamental IR (red arrows). Two 2-photon transitions (XUV ± IR) lead to sidebands (SB_{2q} …) lying between consecutive harmonic peaks ($\text{H}_{2q\pm1}$…). The RABBIT interferometry exploits interferences occuring between the two paths leading to each sideband to get insight on the dynamics of photoemission processes.

$$\text{SB}_{2q} \;=\; \mathcal{A}_{2q} + \mathcal{B}_{2q}\times\cos\left(\Delta\Theta_{2q}\right). \tag{24}$$

The quantities $\mathcal{A}_{2q}$ and $\mathcal{B}_{2q}$ are related to the transition amplitudes introduced in Section II A,

$$\mathcal{A}_{2q} \;\propto\; |\mathcal{T}_{2q-1}|^2 + |\mathcal{T}_{2q+1}|^2 \tag{25}$$

$$\mathcal{B}_{2q} \;\propto\; 2\times|\mathcal{T}_{2q-1}\mathcal{T}_{2q+1}| \tag{26}$$

and $\Delta\Theta_{2q}$ is the difference of phases accumulated by the photoelectron along each of the paths,

$$\Delta\Theta_{2q} \;=\; \Theta_{2q-1} - \Theta_{2q+1}. \tag{27}$$

The RABBIT technique, in its original conception, consists in exploiting these interferences to retrieve the spectral

phase variations of the XUV field, and ultimately reconstruct its temporal profile with attosecond resolution [4]. It relies on the identification of the various contributions to $\Delta\Theta_{2q}$.

2. What is contained in $\Delta\Theta_{2q}$ and what is actually measured

The contributions to $\Delta\Theta_{2q}$ are related to the fields and to the transition operator, as emphasised in section II A. No contribution from the scattering in the final state is *a priori* contained in $\Delta\Theta_{2q}$ since the two "arms" of the interferometer lead by construction to the same final state.

A strong hypothesis of the original RABBIT scheme is that the IR pulse is narrow enough to neglect the integration of the transition amplitudes (Eq. 7). The following derivations also hold if the pulses have finite durations but display constant phases within their bandwidths. It is then possible to isolate the IR pulse contribution, ϕ_{L}, in each of the paths,

$$\Theta_{2q\pm1} \;=\; \mp\phi_{\mathrm{L}} + \vartheta_{2q\pm1}. \tag{28}$$

The sign in front of ϕ_{L} is + if the IR photon is absorbed, − if it is emitted. The term $\vartheta_{2q\pm1}$ is the sum

$$\vartheta_{2q\pm1} \;=\; \phi_{2q\pm1} + \theta_{2q\pm1} \tag{29}$$

of the harmonic phase $\phi_{2q\pm1}$ and of the phase $\theta_{2q\pm1}$ due to the transition operator only, see Eq. 9.

In practice, the experimental setup contains a delay line allowing for a fine control of the time delay $\tau_{\text{XUV-IR}} = \phi_{\mathrm{L}}/\omega_{\mathrm{L}}$ between the XUV and IR pulses (see *e.g.* Fig. 2 and 3 of [9]). A typical RABBIT "trace", obtained by recording a set of electron spectra for a series of delays $\tau_{\text{XUV-IR}}$, displays sideband peaks oscillating at the frequency $2\omega_{\mathrm{L}}$, since $\Delta\Theta_{2q}$ can be recast as

$$\Delta\Theta_{2q} \;=\; 2\omega_{\mathrm{L}} \times \tau_{\text{XUV-IR}} + \underbrace{\vartheta_{2q-1} - \vartheta_{2q+1}}_{\Delta\vartheta_{2q}}. \tag{30}$$

Under conditions allowing for a complete separation of the phase contributions, the so-called "RABBIT phase" $\Delta\vartheta_{2q}$, at the heart of the eponym technique, can be then expressed as

$$\Delta\vartheta_{2q} \;=\; \underbrace{\theta_{2q-1} - \theta_{2q+1}}_{\Delta\theta_{2q}} + \underbrace{\phi_{2q-1} - \phi_{2q+1}}_{\Delta\phi_{2q}}. \tag{31}$$

Until recently, RABBIT was exclusively implemented considering spectrally narrow peaks in the analysed photoelectron spectra. This validates the separation of the contributions to the RABBIT phase (Eq. 31), assumed constant within each peak. In these implementations, the phase measurements are performed on the sideband peaks *integrated spectrally*. However, recent experiments of resonant photoemission in He [35] evidenced sidebands displaying significant structures, the temporal interpretation of which required to resolve the phase variations *within the sideband spectral widths*.

In the following, we will explicitly differentiate the two situations by denoting the phases resolved within the sideband bandwidth as above ($\Delta\vartheta_{2q}$, $\Delta\theta_{2q}$...), and the phases derived from spectrally integrated peaks with barred notations ($\Delta\bar{\vartheta}_{2q}$, $\Delta\bar{\theta}_{2q}$...).

3. Characterisation of attosecond pulse trains

The original implementation of RABBIT assumes the so called "atomic" (or "molecular") phase $\Delta\theta_{2q}$ to be known, or negligible [when the detection gas displays a smooth continuum in the region probed by the XUV photon, see *e.g.* Fig 3(c)]. Thus a measurement of $\Delta\bar{\vartheta}_{2q}$ gives access to the difference of phase $\Delta\bar{\phi}_{2q}$ between two consecutive odd harmonics. Assuming this phase to vary linearly over a spectral range of $2\hbar\omega_{\mathrm{L}}$, the ratio $\Delta\bar{\phi}_{2q}/(2\omega_{\mathrm{L}})$ provides a finite difference evaluation of the group delay characterising the XUV comb. As shown experimentally for the first time in [4], this group delay associated to the so-called "atto-chirp" is identified as the emission time of each harmonic, in line with the strong-field approximation (SFA) for HHG [34]. Since then RABBIT has become a standard method for the characterisation [4] and coherent shaping [11] of attosecond XUV pulses trains, as well as their exploitations based on the "self-probing" paradigm [15], combining simultaneously as- and Å-resolutions.

To summarise, a standard RABBIT setup makes use of two distinct gases: (i) the generation gas, the fingerprints of which are encoded in the emitted XUV radiation and ultimately in the $\Delta\bar{\phi}_{2q}$ contribution to the RABBIT phase; and (ii) a detection gas, which brings the $\Delta\bar{\theta}_{2q}$ contribution. In the following, we review the reinterpretations of the method giving access to the photoemission dynamics through $\Delta\bar{\theta}_{2q}$ ($\Delta\theta_{2q}$ in spectrally resolved, so-called "Rainbow RABBIT", measurements).

B. Transition delay

We present here results of simulations performed on model atom B, that illustrate the principles of the RABBIT method and the way it provides insight on 2-photon transition dynamics. These simulations do not account for the limitations inherent to experimental conditions, such as the incomplete characterisation of the ionising pulses, stability issues or the finite resolution of detectors. They represent "ideal" RABBIT numerical experiments, showing what the technique may *at best* give access to.

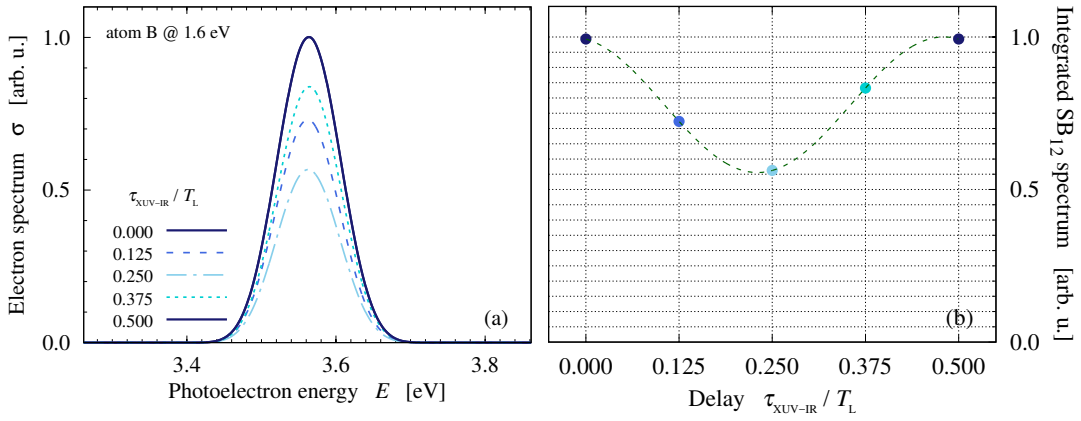

FIG. 5: (color online) (a) SB_{12} spectrum obtained with atom B in presence of H_{11}, H_{13} and the fundamental IR at $\hbar\omega_\mathrm{L} = 1.60$ eV for values of the delay $\tau_{\mathrm{XUV\text{-}IR}}$ ranging from 0 to $0.5 \times T_\mathrm{L}$ ($T_\mathrm{L} = 2\pi/\omega_\mathrm{L}$). (b) Integrated SB_{12} intensity as a function of the delay $\tau_{\mathrm{XUV\text{-}IR}}$ (blue circles). Fitting these data with the generic function given in Eq. 32 (green dashed curve) provides a measure of the RABBIT phase $\Delta\bar{\vartheta}_{12} = 0.08 \times \pi$ rad.

1. *Transition phases*

We simulated RABBIT on atom B initially in its ground state. We first detail the results obtained with a fundamental laser central frequency $\hbar\omega_\mathrm{L} = 1.60$ eV, such that H_{11} reaches the resonance lying at 1.86 eV above threshold, already investigated in section III B 1. Our analysis focuses on SB_{12}, resulting from the 2-photon paths H_{11}+IR and $\mathrm{H}_{13}-$IR, for which we computed the transition phases (θ_{11} and θ_{13} respectively) using second order perturbation theory (Eq 9 with $\phi_a \equiv \phi_{11/13} = 0$ and $\phi_b \equiv \phi_\mathrm{L} = 0$) on the one hand, and performed a RABBIT analysis from time-dependent simulations on the other hand.

The 3-color light pulses were defined according to Eq. 17 with $\omega_k = k \times \omega_\mathrm{L}$ ($k = 1, 11, 13$). Here as well, the time-domain CEP $\tilde{\phi}_k$ were all set to 0. The XUV envelops were centered at the time origin ($\tau_{11} = \tau_{13} = 0$) while the center of the IR pulse was assigned the role of adjustable delay, $\tau_1 = \tau_{\mathrm{XUV\text{-}IR}}$. The pulses durations were all set to $15 \times 2\pi/\omega_\mathrm{L}$ FWHM (~ 40 fs FWHM). The field strengths were set low enough to keep negligible any process involving more than 2 photons.

Figure 5(a) shows the electron spectrum σ centered on the SB_{12} peak, obtained in time-dependent simulations for 5 values of $\tau_{\mathrm{XUV\text{-}IR}}$ ranging from 0 to $0.5 \times 2\pi/\omega_\mathrm{L}$. The peak oscillation is clearly pronounced. The *integrated* peak intensity is displayed in 5(b) as a function of $\tau_{\mathrm{XUV\text{-}IR}}$ (circles). The RABBIT phase $\Delta\bar{\vartheta}_{12}$ characterising these oscillations, evaluated by fitting the data to the generic function (dashed curve)

$$g(\tau_{\mathrm{XUV\text{-}IR}}) \;=\; \mathcal{A} + \mathcal{B} \times \cos(2\omega_\mathrm{L} \times \tau_{\mathrm{XUV\text{-}IR}} + \Delta\bar{\vartheta}_{12}), \quad (32)$$

amounts to $0.08 \times \pi$ rad. We also applied the fitting procedure to each photoelectron energy within the support of SB_{12}. The spectrally resolved RABBIT phase, $\Delta\vartheta_{12}$, is displayed in Fig. 6 (green circles) together with the averaged peak intensity (given by $\mathcal{A}$ in the fitting procedure, see Eq. 32). The phase $\Delta\vartheta_{12}$ is not constant: It varies by $\simeq 0.1 \times \pi$ rad over the SB_{12} bandwidth. However, its linear trend suggests that a single group delay will be sufficient to characterise the photoemission dynamics, as will be confirmed further.

In addition, we computed the transition phases θ_{11} and θ_{13} associated with the two different paths leading to SB_{12} for each final energy E, using perturbation theory (Eqs 2–9). Their difference $\theta_{11} - \theta_{13} = \vartheta_{11} - \vartheta_{13}$ is reported in Fig. 6 (yellow crosses) as a function of E. It effectively coincides, within the numerical accuracy, with the "measured" spectrally resolved RABBIT phase $\Delta\vartheta_{12}$ all over the peak width. Note that the phase of the integrated peak, $\Delta\bar{\vartheta}_{12}$ (dashed horizontal line) is nevertheless representative of the wave packet, since it is equal to the phase $\Delta\vartheta_{12}$ evaluated at the photoelectron average energy $\bar{E}$ (vertical line). This is because the resonance is scanned by a narrow pulse ($\simeq 100$ meV FWHM) compared to its natural width ($\hbar\Gamma_\mathrm{R}^{-1} \simeq 400$ meV). We repeated the procedure for a series of laser central energies $\hbar\omega_\mathrm{L}$ ranging from 1.50 eV to 1.65 eV. Figure 7(a) shows the RABBIT phases $\Delta\vartheta_{12}(\bar{E})$ (red circles) as well as the phase difference $\Delta\theta_{12}(\bar{E}) = \theta_{11}(\bar{E}) - \theta_{13}(\bar{E})$ from the perturbative computations (yellow crosses), evaluated at the mean photoelectron energy $\bar{E}$ for each simulated ω_L. As expected, the phase difference undergoes a significant jump while H_{11} crosses the resonance, corresponding to a laser central energy $\hbar\omega_\mathrm{L} = (E_\mathrm{R} - E_0)/11 \simeq 1.59$ eV.

The agreement between $\Delta\vartheta_{12}$ and $\Delta\theta_{12}$ is perfect over the whole considered range. These results highlight the validity of the RABBIT interferometric scheme to measure 2-photon transition phase differences. We have seen in section III how the group delay associated with the latter was representative of the 2-photon transition dynamics. Hereafter, we combine these conclusions and clarify the link between RABBIT phase, which is an experimentally measurable quantity, and transition dynamics.

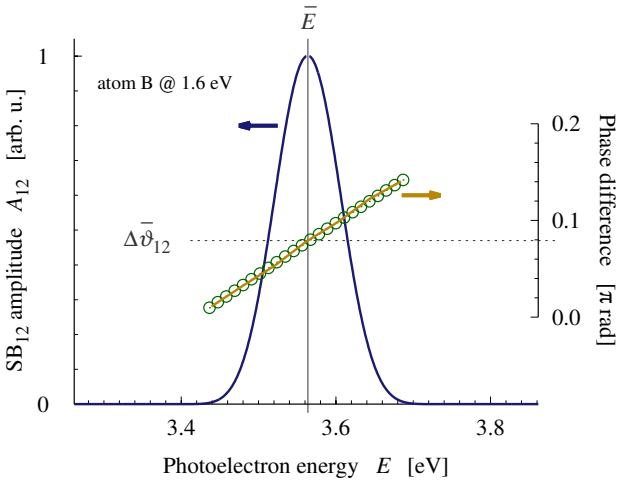

FIG. 6: (color online) Spectrally resolved RABBIT analysis of SB_{12} (ω_L = 1.60 eV) in atom B: sideband amplitude $\mathcal{A}_{12}$ (full blue curve); RABBIT phase $\Delta\vartheta_{12}$ obtained with time-dependent simulations (green circles); transition phase difference $\Delta\theta_{12} = \theta_{11} - \theta_{13}$ obtained with second order perturbation theory (yellow curve). $\bar{E}$ is the average energy under SB_{12} (vertical line) and $\Delta\bar{\vartheta}_{12}$ is the RABBIT phase derived from the *integrated* sideband (horizontal line, see also Fig. 5).

2. *Accurate and approximate evaluations of transition delays*

The relevance of the group delay $\hbar\partial\theta/\partial E$ to characterise the transition dynamics (Section III) on the one hand and the direct link between transition phase θ and RABBIT phase $\Delta\vartheta$ (Section IV B 1 above) on the other hand suggest to compare the group delay associated with $\Delta\vartheta$ to the EWP dynamics revealed by the flux analysis in the time domain.

We have therefore simulated ionisation of atom B in the same conditions as above, but considering the two paths leading to SB_{12} independantly: One first set of simulations was performed in the simultaneous presence of the IR and H_{11} only, and a second one in the simultaneous presence of the IR and H_{13} only. In each of the paths, we have characterised the ionisation dynamics with the flux analysis (Eqs. 22-23) of the 2-photon EWP produced at the SB_{12} energy, providing numerical times of flight ToF_{11} and ToF_{13} respectively. These data allows an evaluation of the transition delay *difference* through the two paths associated with SB_{12} as

$$\Delta ToF_{12} = ToF_{11} - ToF_{13}. \tag{33}$$

The results are shown in Fig. 7(b), as a function of $\hbar\omega_L$ (red full circles). The increase of ΔToF_{12} near the central laser energy $\hbar\omega_L \simeq 1.59$ eV reflects the delay induced by the transition through the intermediate resonance in the $H_{11} + IR$ path, the alternative path involving H_{13} through a smooth continuum endorsing the role of reference.

We then computed the group delay associated with the

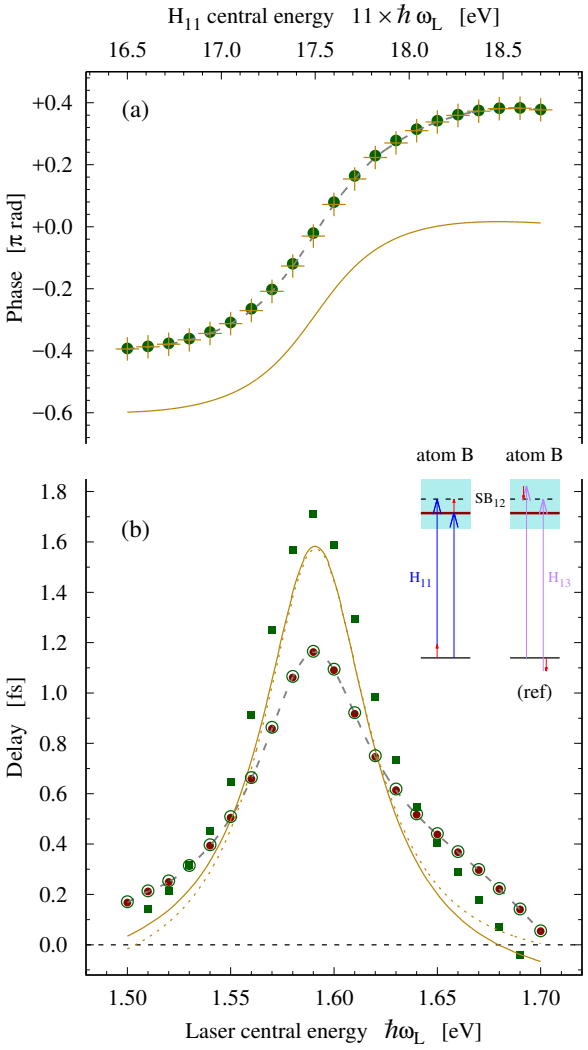

FIG. 7: (color online) (a) SB_{12} transition phase difference in atom B as a function of the fundamental laser energy $\hbar\omega_L$ (the corresponding H_{11} energies are given in the upper axis): RABBIT phase $\Delta\bar{\vartheta}_{12}$ (green circles); transition phase difference $\Delta\theta_{12} = \theta_{11} - \theta_{13}$ evaluated at the average sideband energy $\bar{E}$ for each ω_L using second order perturbation theory (yellow crosses). The yellow curve shows the scattering phase difference $\eta_{11} - \eta_{13}$ computed for each ω_L. (b) Transition delay difference between the H_{11} +IR and H_{13}-IR paths: time of flight difference $\Delta ToF_{12} = ToF_{11} - ToF_{13}$ (red full circles); RABBIT group delay τ_{12} as defined in Eq. 34 (green empty circles); approximate RABBIT group delay $\bar{\tau}_{12}$ as defined in Eq. 35 (green rectangles). The yellow full curve is the weighted scattering delay difference $11/12 \times \tau_{sc}^{(11)} - 13/12 \times \tau_{sc}^{(13)}$, and the yellow dotted curve is the resonant term $11/12 \times \tau_{sc}^{(11)}$ (scattering delays from [24]). The grey dashed curves serve as guidelines.

RABBIT phase,

$$\tau_{12} = \hbar \left.\frac{\partial\Delta\vartheta_{12}}{\partial E}\right|_{\bar{E}}, \tag{34}$$

at the average photoelectron energy associated with SB_{12} for each ω_L. They are also displayed in Fig. 7(b) (green

empy circles). The perfect agreement obtained between τ_{12} and ΔToF_{12} confirms the conclusions drawn when comparing ToF differences with formal group delays in a series of 2-photon transitions on the one hand (see Fig. 3) and transition phase difference with RABBIT phases on the other hand [see Figs. 6 and 7(a)].

In addition, we have tested the approximate evaluation of the group delay associated with the RABBIT phase suggested by Eq. 13 – invoked for example when the experimental detection is not precise enough to resolve the RABBIT phase variations within the sidebands. In the present context, this approximate group delay reads [36, 37]

$$\bar{\tau}_{12} \;=\; \frac{1}{12}\frac{\partial\Delta\bar{\vartheta}_{12}}{\partial\omega_{\rm L}}. \tag{35}$$

We computed $\bar{\tau}_{12}$ using the data sampled in Fig. 7(a) (green circles) and displayed the result in Fig. 7(b) (green rectangles). While it qualitatively follows the trend of the exact group delay, with a maximum reached when H_{11} hits the intermediate resonance, it fails to accurately reproduce the latter due to the various approximations invoked to derive its expression (see Section II B).

These results emphasise the importance to resolve the RABBIT phase variations within each sideband to accurately access the transition dynamics. It is however important to realise that the impact of the approximations strongly depends on the probed system and on the pulse parameters.

In [38], He atoms were ionised by an XUV beam generated in Ar. The central energy $\hbar\omega_{\rm L}$ of the generating laser was set around 1.54 eV, with a tunability of $\sim$ 10 meV. Varying thereby $\hbar\omega_{\rm L}$ allowed the 15^{th} harmonic to scan the $1s3p$ level of He over $\sim$ 200 meV, with the sideband next up (SB_{16}) lying safely in the continuum. RABBIT measurements evidence a transition phase $\Delta\bar{\theta}_{16}$ undergoing a jump of $\sim 0.5\pi$. In this case, the measured phase variations are obviously affected by the pulse widths, since the phase of a 2-photon transition through a discrete (bound) intermediate state is expected to display a sharp π rad jump when considering monochromatic fields. This work is one the first investigations of intrinsic photoemission dynamics using RABBIT. Although the time domain interpretation of the measurements was not pushed further in this seminal work, the spectral phase variations constitute a clear signature of the influence of the intermediate $1s3p$ resonance on the 2-photon transition dynamics.

In a different study [36], RABBIT measurements were simulated in a model N_2, following vibronically resolved experiments and a preliminary interpretation reported in [18]. Two resonances corresponding to the first two vibrational states of an electronic resonance in the X channel were scanned by H_{11} of a laser with a simulated tunability of approximately ± 0.025 eV around $\hbar\omega_{\rm L} = 1.56$ eV. The computed vibrationally-resolved SB_{12} RABBIT phases display a clear phase jump each time H_{11} crosses a resonance, with an additional intermediate sharp π jump resulting from destructive interferences between the two consecutive resonances in one of the vibrational channels. These phase variations were interpreted in the time domain using Eq. 34, and compared to the "actual" ionisation dynamics using numerical ToF like in the present study, with again a satisfactory agreement.

C. Scattering delay

In this last part, we review the possibilities to access *scattering* delays out of RABBIT measurements. Three different (yet related) methods, established at different levels of approximation, will be considered. They are introduced below according to the gradual complexity of their experimental implementations. The first method relies on a standard measurement of *integrated* RABBIT phases $\Delta\bar{\vartheta}_{2q}$. The second one is based on the variations of $\Delta\bar{\vartheta}_{2q}$ with respect to $\omega_{\rm L}$ and therefore requires a laser frequency scan. The last one, dubbed "Rainbow RABBIT", uses the spectral variations of $\Delta\vartheta_{2q}(E)$ within the sideband and therefore requires measurements with high spectral resolution as well as an ideally narrow IR probe pulse. The three methods have different ranges of applicability. The second one is particularly suited to the RABBIT simulations we performed in atom B, as will be illustrated.

1. *Approximate evaluations of scattering delays using $\Delta\bar{\vartheta}_{2q}$ (standard RABBIT)*

The possibility to access photoelectron *scattering* delays experimentally with the RABBIT scheme was first demonstrated in [16]. It was established in this work that the two-photon transition phase for each path leading to a given SB_{2q} is equal to the scattering phase $\eta_{2q\pm1}$ in the intermediate continuum state, computed at the harmonic peak central energies

$$E_{2q\pm1} \;=\; E_0 + (2q \pm 1) \times \hbar\omega_{\rm L}, \tag{36}$$

up to a universal correction $\phi_{\rm CC}^{(\pm)}$. The latter accounts for the couplings between the intermediate and final continuum states, induced by the IR "probe" through the asymptotic Coulomb tail of the ionic core potential. $\phi_{\rm CC}^{(\pm)}$ possesses an analytic expression valid at sufficiently high energies, see [39]. The $\Delta\bar{\theta}_{2q}$ contribution to a given sideband then reads:

$$\Delta\bar{\theta}_{2q} \;=\; \eta_{2q-1} - \eta_{2q+1} + \Delta\phi_{\rm CC} \tag{37}$$

with $\Delta\phi_{\rm CC} = \phi_{\rm CC}^{(-)} - \phi_{\rm CC}^{(+)}$. Measuring $\Delta\bar{\theta}_{2q}$ hence provides a finite-difference evaluation of the scattering delay

$$\tau_{\rm sc}(E_{2q}) \;=\; \hbar\,\frac{\partial\eta_{\rm sc}}{\partial E}\bigg|_{E_{2q}} \tag{38}$$

associated with a (virtual) 1-photon ionisation towards $E_{2q} = E_0 + 2q \times \hbar\omega_L$, since

$$\frac{\Delta\bar{\theta}_{2q}}{2\times\omega_L} = \underbrace{\frac{\eta_{2q-1}-\eta_{2q+1}}{2\times\omega_L}}_{\simeq\tau_{sc}(E_{2q})} + \frac{\Delta\phi_{CC}}{2\times\omega_L}. \quad (39)$$

This link between $\Delta\bar{\theta}_{2q}$ and $\tau_{sc}(E_{2q})$, which was invoked in numerous subsequent theoretical and experimental studies (see *e.g.* [31, 40–48] for a non exhaustive list), holds if the continuum is smooth enough for the scattering phase to vary linearly within an energy range of $2\times\hbar\omega_L$. Below, we show that our simulations in atom B suggest an alternative interpretation of RABBIT phases in terms of scattering delays, adapted for transitions through structured continua as well.

2. … using $\partial\Delta\bar{\vartheta}_{2q}/\partial\omega_L$

Let's turn back to the SB_{12} RABBIT phases "measured" in atom B. We will only consider in the following the "integrated" phase measurements, displayed in Fig. 7(a). We have previously seen that the variations of $\Delta\bar{\vartheta}_{12}$ with respect to ω_L were partly representative of the *transition* dynamics, according to Eq. 35. We will now alternatively extract, from the same RABBIT phases, insight on the *scattering* dynamics, basing our analysis on Eq. 37 instead.

For each considered ω_L, we have computed the scattering phases η_{11} and η_{13} of the continuum states reached at the central harmonic peak energies E_{11} and E_{13} (Eq. 36). Their difference $\eta_{11}-\eta_{13}$ is displayed in Fig 7(a) as a function of ω_L (yellow full curve), for a direct comparison with the RABBIT phases (green circles). In the present situation, the behaviour of the scattering phase difference is governed by the resonant one, η_{11} (we checked that η_{13} is nearly flat). While an ideally narrow and isolated resonance would result in a sharp π rad jump, the computed phase follows a jump spread over $\Gamma_R \simeq 0.40$ eV and attenuated by the contribution of the background continuum (it spans $\simeq 0.6\times\pi$ rad).

Keeping in mind that the RABBIT phase $\Delta\bar{\vartheta}_{12}$ is a direct measure of the transition phase difference $\Delta\bar{\theta}_{12}$ (the harmonic field phases were set to 0), we conclude from Eq. 37 that the difference between $\Delta\bar{\vartheta}_{12}$ and $\eta_{11}-\eta_{13}$ is the "continuum-continuum" correction $\Delta\phi_{CC}$. In this case, it evolves nearly linearly from $\sim 0.2\times\pi$ rad to $\sim 0.4\times\pi$ rad over the covered range[4]. In this context, the SB_{12} group delay $\bar{\tau}_{12}$ defined in Eq. 35 can be recast as

$$\frac{1}{12}\frac{\partial\Delta\bar{\vartheta}_{12}}{\partial\omega_L} = \frac{1}{12}\frac{\partial(\eta_{11}-\eta_{13})}{\partial\omega_L} + \frac{1}{12}\frac{\partial\Delta\phi_{CC}}{\partial\omega_L}$$
$$= \frac{11}{12}\underbrace{\frac{\partial\eta_{11}}{\partial(11\times\omega_L)}}_{\tau_{sc}^{(11)}} - \frac{13}{12}\underbrace{\frac{\partial\eta_{13}}{\partial(13\times\omega_L)}}_{\tau_{sc}^{(13)}} + \frac{1}{12}\frac{\partial\Delta\phi_{CC}}{\partial\omega_L} \quad (40)$$

where $\tau_{sc}^{(2q\pm1)}$ are the scattering delays in the continuum states populated upon absorption of the harmonics at the energies $E_{2q\pm1}$ (Eq. 36), and

$$\frac{\partial\Delta\phi_{CC}}{\partial\omega_L} \sim 1 \text{ fs} \quad (41)$$

in our simulations.

We have thus obtained an alternative interpretation of the RABBIT delay $\bar{\tau}_{12}$ first introduced in Eq. 35. The weighted scattering delay difference $11/12\times\tau_{sc}^{(11)} - 11/13\times\tau_{sc}^{(13)}$ is displayed in Fig. 7(b) (yellow full curve). It follows nicely the RABBIT delay (green rectangles in Fig. 7), especially near resonance ($\omega_L \simeq 1.59$ eV), with a global time shift of ~ 100 as due to the linear chirp of $\Delta\phi_{CC}$ (see Eq. 41). To further confirm the preponderant role of the resonant transition (through H_{11}) over the alternative one (through H_{13}), we have also displayed in Fig. 7(b) the weighted scattering delay $11/12\times\tau_{sc}^{(11)}$ alone (dotted yellow curve). It is indeed very close to the weighted delay difference (full yellow curve) – nearly equal at resonance. Note that at larger orders q, the ratios $(2q\pm1)/(2q)$ converge to 1 and the spectral derivative of $\Delta\phi_{CC}$ vanishes. These quantities can then be practically neglected from Eq. 40 and the methods gives a direct access to the scattering delay difference $\tau_{sc}^{(2q-1)} - \tau_{sc}^{(2q+1)}$. Probing resonant scattering dynamics with this interpretation of *integrated* RABBIT measurements was successfully achieved in the $3s^{-1}4p$ Fano resonance of Ar [49].

3. … and using $\partial\Delta\vartheta_{2q}(E)/\partial E$ (*Rainbow* RABBIT)

Eventually, we show how scattering dynamics can be accurately retrieved from *spectrally resolved* RABBIT measurement. Here as well, we use the formalism introduced in [16, 39]. Eq. 37 allows to rewrite the spectrally resolved RABBIT phase as

$$\Delta\vartheta_{2q}(E) = \eta_{sc}(E-\hbar\omega_L) + \eta_{sc}(E+\hbar\omega_L) - \Delta\phi_{CC}(E). \quad (42)$$

Only the central frequency of the IR, ω_L, is considered in this expression. This implies that the IR pulse is spectrally narrow enough to neglect the integration (Eq. 7) that would blur the η_{sc} imprints in $\Delta\vartheta_{2q}(E)$. The two wave packets contributing to the SB are then considered as spectrally shifted replica of the 1-photon electron wave packets created by each harmonic.

[4] The universal analytic formula given in [39] is not expected to be valid at such a near-threshold energy. Computed in the present case, it presents a spurious linear chirp of ~ -0.3 fs (not shown).

The link with the scattering delays is then straightforward. It is simply given by the spectral derivative of Eq. 42,

$$\hbar\frac{\partial\Delta\vartheta_{2q}(E)}{\partial E} = \tau_{\rm sc}(E-\hbar\omega_{\rm L}) - \tau_{\rm sc}(E+\hbar\omega_{\rm L}) + \hbar\frac{\partial\Delta\phi_{\rm CC}(E)}{\partial E}. \quad (43)$$

Accessing the scattering dynamics from Rainbow RABBIT measurements thus requires approximations only on the spectral derivative of the $\Delta\phi_{\rm CC}$ correction – for example assumed negligible, or computed using the analytic formula given in [39]. Note that it allows retrieving the complete scattering dynamics beyond the limiting notion of group delay, when the RABBIT phase undergoes significantly non linear variations within the SB bandwidth. This was demonstrated and first applied in [35] to accurately reconstruct the autoionisating dynamics of He excited in its $2s2p$ state, where it was shown that *integrated* RABBIT measurements were not adapted.

V. CONCLUSION

We have shown how the formal group delay derived from the phase associated with the transition operator in 2-photon ionisation (the so-called transition phase) is representative of the actual photoelectron dynamics, using numerical simulations on model atoms. Our simulations performed on model atoms displaying smooth or structured continua illustrate the role of the intermediate states reached along the transition. The group delay may be interpreted as a transition "duration" only when a resonance with significant lifetime is transiently populated during the process.

We then illustrated how XUV + IR RABBIT interferometry gives access to the transition phase and to the dynamics it encodes. Our numerical experiments emphasise the importance of resolving the RABBIT phases within the photoelectron wave packet bandwidth, using the so-called Rainbow RABBIT approach, to retrieve the transition dynamics accurately. Measurements based on the standard RABBIT scheme (which measures a global phase of the wave packet) provide insight on those dynamics only qualitatively.

Finally, we reviewed the ways of using RABBIT (in various reinterpretations) to access the more fundamental *scattering* dynamics, which affects any photoelectron in the final stage of its emission, as it scatters away under the influence of the remaining ionic core. Three methods, tested in experiments in the last few years, were considered. All rely on an expression of the 2-photon transition phase involving the scattering phase in the intermediate continuum state reached by the XUV– augmented by the so-called "continuum-continuum" correction accounting for the IR induced Coulomb coupling of the intermediate and final continuum states. The first two methods use the measurements of standard (integrated) RABBIT phases. In the first one, scattering delays are deduced from the RABBIT phases themselves, while in the one second the delays are related to the RABBIT phase *variations* against the fundamental IR laser frequency. The third method is based on Rainbow RABBIT measurements, where the scattering dynamics is reconstructed from the spectral evolution of the RABBIT phase within the photoelectron wave packet bandwidth. Each of the three approaches requires an adapted experimental setup, with variable complexities (fixed *vs.* tunable IR frequency, standard *vs.* high spectral resolution). One should keep in mind that all these approaches rely on different approximations, with various sensitivities to characteristic parameters – such as the ionising pulse durations and the presence of resonances in the probed region of the continuum.

We acknowledge financial support from the LABEXs MiCheM and PlasPar (ANR-11-IDEX-0004-02) and the program ANR-15-CE30-0001-01-CIMBAAD. We are grateful to Luca Argenti, Lou Barreau, Bertrand Carré, Jan Marcus Dahlström, Baptiste Fabre, Álvaro Jiménez-Galán, Stephan Haessler, Anne L'Huillier, Yann Mairesse, Fernando Martìn, Thierry Ruchon and Pascal Salières for stimulating and fruitful interactions at all stages of our immersion in the domain of photoemission delays.

[1] P. Agostini and L. F. DiMauro, The physics of attosecond light pulses, Rep. Prog. Phys. **67**, 813–55 (2004).
[2] F. Krausz and M. Ivanov, Attosecond physics, Rev. Mod. Phys. **81**, 163 (2009).
[3] M. Hentschel, R. Kienberger, Ch. Spielmann, G. A. Reider, N. Milosevic, T. Brabec, P. Corkum, U. Heinzmann, M. Drescher and F. Krausz, Attosecond metrology, Nature**414**, 509 (2001).
[4] P. M. Paul, E. S. Toma, P. Breger, G. Mullot, F. Augé, Ph. Balcou, H. G. Muller and P. Agostini, Observation of a Train of Attosecond Pulses from High Harmonic Generation, Science **292**, 1689–92 (2001).
[5] M. Ferray, A. L'Huillier, X. F. Li, L. A. Lompre, G. Mainfray and C. Manus, Multiple-harmonic conversion of 1064 nm radiation in rare gases, J. Phys. B: At. Mol. Opt. Phys. **21**, L31 (1988).
[6] A. McPherson, G. Gibson, H. Jara, U. Johann, T. S. Luk, I. A. McIntyre, K. Boyer and C. K. Rhodes, Studies of multiphoton production of vacuum-ultraviolet radiation in the rare gases, J. Opt. Soc. Am. B **4**, 595 (1987).
[7] Y. Mairesse and F. Quéré, Frequency-resolved optical gating for complete reconstruction of attosecond bursts,, Phys. Rev. A **71**, 011401 (2005).
[8] V. S. Yakovlev and F. Bammer and A. Scrinzi, Attosec-

ond streaking measurements, J. Mod. Opt. **52**, 395–410 (2005)

[9] Y. Mairesse, A. de Bohan, L. J. Frasinski, H. Merdji, L. C. Dinu, P. Monchicourt, P. Breger, M. Kovačev, R. Taïeb, B. Carré, H. G. Muller, P. Agostini and P. Salières, Attosecond Synchronization of High-Harmonic Soft X-rays, Science **302**, 1540–3 (2003).

[10] H. G. Muller, Reconstruction of attosecond harmonic beating by interference of two-photon transitions, Applied Physics B **74**, s17–s21 (2002).

[11] W. Boutu, S. Haessler, H. Merdji, P. Breger, G. Waters, M. Stankiewicz, L. J. Frasinski, R. Taïeb, J. Caillat, A. Maquet, P. Monchicourt, B. Carré, P. Salières, Coherent control of attosecond emission from aligned molecules, Nature Physics **4** 545, (2008).

[12] S. Chatziathanasiou, S. Kahaly, E. Skantzakis, G. Sansone, R. Lopez-Martens, S. Haessler, K. Varju, G. D. Tsakiris, D. Charalambidis and P. Tzallas, Generation of Attosecond Light Pulses from Gas and Solid State Media, Photonics **4**, 26 (2017).

[13] M. Chini, K. Zhao and Z. Chang, The generation, characterization and applications of broadband isolated attosecond pulses, Nature Photonics **8**, 176-86 (2014).

[14] E. Mansten, J. M. Dahlström, P. Johnsson, M. Swoboda, A. LHuillier and J. Mauritsson, New J. Phys. **10**, 083041 (2008).

[15] S. Haessler, J. Caillat and P. Salières, Self-probing of molecules with high harmonic generation, J. Phys. B: At. Mol. Opt. Phys.**44**, 203001 (2011).

[16] K. Klünder, J. M. Dahlström, M. Gisselbrecht, T. Fordell, M. Swoboda, D. Guénot, P. Johnsson, J. Caillat, J. Mauritsson, A. Maquet, R. Taïeb and A. L'Huillier, Probing Single-Photon Ionization on the Attosecond Time Scale, Phys. Rev. Lett. **106**, 143002 (2011).

[17] M. Schultze *et al.*, Delay in Photoemission, Science **328**, 1658–62 (2010).

[18] S. Haessler, B. Fabre, J. Higuet, J. Caillat, T. Ruchon, P. Breger, B. Carré, E. Constant, A. Maquet, E. Mével, P. Salières, R. Taïeb, and Y. Mairesse, Phase-resolved attosecond near-threshold photoionization of molecular nitrogen, Phys. Rev. A **80**, 011404(R) (2009).

[19] A. L. Cavalieri *et al.*, Attosecond spectroscopy in condensed matter, Nature **449**, 1029 (2007).

[20] E. P. Wigner, Lower Limit for the Energy Derivative of the Scattering Phase Shift, Phys. Rev. **98**, 145–7 (1955).

[21] J. M. Dahlström, M. Vacher, A. Maquet, J. Caillat and S. Haessler, Photoionization Time Delays, in *Ultrafast Dynamics Driven by Intense Light Pulses* edited by M. Kitlzer and S. Gräfe, Springer Series on Atomic, Optical, and Plasma Physics **86**, (Springer International Publishing Switzerland), 177–202 (2016).

[22] A. Maquet, J. Caillat and R. Taïeb, Attosecond delays in photoionization: time *and* quantum mechanics, J. Phys. B: At. Mol. Opt. Phys. **47**, 204004 (2014).

[23] R. Pazourek, S. Nagele and J. Burgdörfer, Attosecond chronoscopy of photoemission, Rev. Mod. Phys. **87**, 765–802 (2015).

[24] R. Gaillac, M. Vacher, A. Maquet, R. Taïeb and J. Caillat, Attosecond photoemission dynamics encoded in real-valued continuum wave functions, Phys. Rev. A **43**, 093410 (2016).

[25] D. Loomba, S. Wallace, D. Dill and J. L. Dehmer, Pictures of unbound molecular electrons, including shape-resonant states. Eigenchannel contour maps, J. Chem. Phys. **75**, 4546–52 (1981).

[26] Á. Jiménez-Galán, L. Argenti and F. Martín, Modulation of Attosecond Beating in Resonant Two-Photon Ionization, Phys. Rev. Lett. **113**, 263001 (2014).

[27] J. M. Dahlström, A. L'Huillier and A. Maquet, Introduction to attosecond delays in photoionization, J. Phys. B: At. Mol. Opt. Phys. **45**, 183001 (2012).

[28] F. Gel'mukhanov and H. Ågren, Resonant X-ray Raman scattering, Physics Reports **312**, 87-330 (1999).

[29] M. Simon, L. Journel, R. Guillemin, W. C. Stolte, I. Minkov, F. Gel'mukhanov, P. Sałek, H. Ågren, C. Carniato, R. Taïeb, A. C. Hudson, and D. W. Lindle, Femtosecond nuclear motion of HCl probed by resonant x-ray Raman scattering in the Cl 1*s* region, Phys. Rev. A**73**, 020706 (2006).

[30] E. S. Toma and H. G. Muller, Calculation of matrix elements for mixed extreme-ultraviolet–infrared two-photon above-threshold ionization of argon, J. Phys. B: At. Mol. Opt. Phys. **35**, 3435 (2002).

[31] L. Argenti, Á. Jiménez-Galán, J. Caillat, R. Taïeb, A. Maquet, and F. Martín, Control of photoemission delay in resonant two-photon transitions, Phys. Rev. A **95**, 043426 (2017).

[32] K. C. Kulander, K. J. Schaffer and J. L. Krause, Time-dependent studies of multiphoton processes, in *Atoms in Intense Laser Fields* edited by M. Gavrila, Academic Press, 247, (1992).

[33] V. Véniard, R. Taïeb and A. Maquet, Phase dependence of $(N+1)$-color $(N>1)$ IR-UV photoionization of atoms with higher harmonics, Phys. Rev. A **54**, 721 (1996).

[34] M. Lewenstein, Ph. Balcou, M. Yu. Ivanov, A. L'Huillier and P. B. Corkum, Theory of high-harmonic generation by low-frequency laser fields, Phys. Rev. A **49**, 2117–32 (1994).

[35] V. Gruson, L. Barreau, Á. Jiménez-Galan, F. Risoud, J. Caillat, A. Maquet, B. Carré, F. Lepetit, J.-F. Hergott, T. Ruchon, L. Argenti, R. Taïeb, F. Martín and P. Salières, Attosecond dynamics through a Fano resonance: Monitoring the birth of a photoelectron, Science **354**, 734–8 (2016).

[36] J. Caillat, A. Maquet, S. Haessler, B. Fabre, T. Ruchon, P. Salières, Y. Mairesse, and R. Taïeb, Attosecond Resolved Electron Release in Two-Color Near-Threshold Photoionization of N_2, Phys. Rev. Lett. **106**, 093002 (2011).

[37] R. Guichard, J. Caillat, S. Haessler, Ž. Diveki, T. Ruchon, P. Salières, R. Taïeb, and A. Maquet, Attosecond molecular spectroscopies with XUV harmonic radiation, in *Attosecond physics* edited by L. Plaja *et al*, Springer Series in Optical Science **177**, 191 (2013).

[38] M. Swoboda, T. Fordell, K. Klünder, J. M. Dahlström, M. Miranda, C. Buth, K. J. Schafer, J. Mauritsson, A. L'Huillier and M. Gisselbrecht, Phase Measurement of Resonant Two-Photon Ionization in Helium, Phys. Rev. Lett. **104**, 103003 (2010).

[39] J. M. Dahlström, D. Guénot, K. Klünder, M. Gisselbrecht, J. Mauritsson, A. L'Huillier, A. Maquet and R. Taïeb, Theory of attosecond delays in laser-assisted photoionization, Chem. Phys. **414**, 53-64 (2013)

[40] A. Kumar, H. R. Varma, P. C. Deshmukh, S. T. Manson, V. K. Dolmatov, and A. Kheifets, Wigner photoemission time delay from endohedral anions, Phys. Rev. A **94**, 043401 (2016).

[41] E. Lindroth and J. M. Dahlström, Attosecond delays in laser-assisted photodetachment from closed-shell negative ions,, Phys. Rev. A **96**, 013420 (2017).

[42] T. Barillot, C. Cauchy, P.-A. Hervieux, M. Gisselbrecht, S. E. Canton, P. Johnsson, J. Laksman, E. P. Mansson, J. M. Dahlström, M. Magrakvelidze, G. Dixit, M. E. Madjet, H. S. Chakraborty, E. Suraud, P. M. Dinh, P. Wopperer, K. Hansen, V. Loriot, C. Bordas, S. Sorensen, and F. Lépine, Angular asymmetry and attosecond time delay from the giant plasmon resonance in C_60 photoionization, Phys. Rev. A **91** 033413 (2015).

[43] D. Baykusheva and H. J. Wörner, Theory of attosecond delays in molecular photoionization, J. Chem. Phys. **146**, 124306 (2017).

[44] L. Cattaneo, J. Vos, M. Lucchini, L. Gallmann, C. Cirelli, and U. Keller, Comparison of attosecond streaking and RABBITT, Opt. Express **24**, 29060–76 (2016).

[45] S. Heuser, Á. Jiménez Galán, C. Cirelli, C. Marante, M. Sabbar, R. Boge, M. Lucchini, L. Gallmann, I. Ivanov, A. S. Kheifets, J. M. Dahlstrm, E. Lindroth, L. Argenti, F. Martn, and U. Keller, Angular dependence of photoemission time delay in helium, Phys. Rev. A **94**, 063409 (2016).

[46] P. Hockett, E. Frumker, D. M. Villeneuve and P. B. Corkum, Time delay in molecular photoionization, J. Phys. B: At. Mol. Opt. Phys. **49**, 095602 (2016).

[47] M. Huppert, I. Jordan, D. Baykusheva, A. von Conta and H. J. Wörner, Attosecond delays in molecular photoionization, Phys. Rev. Lett. **117**, 093001 (2016).

[48] I. A. Ivanov and A. S. Kheifets, Angle-dependent time delay in two-color XUV+IR photoemission of He and Ne, Phys. Rev. A **96**, 013408 (2017).

[49] M. Kotur, D. Guénot, Á. Jiménez-Galán, D. Kroon, E. W. Larsen, M. Louisy, S. Bengtsson, M. Miranda, J. Mauritsson, C. L. Arnold, S. E. Canton, M. Gisselbrecht, T. Carette, J. M. Dahlström, E. Lindroth, A. Maquet, L. Argenti, F. Martín and A. L'Huillier, Spectral phase measurement of a Fano resonance using tunable attosecond pulses, Nature Communications **7**, 10566 (2016).